




Investigation the Performance of Cr-Doped ZnO Nanocrystalline Thin Film in Photodiode Applications

A. TURSUCU,¹ S. AYDOGAN,^{2,3} A. KOCYIGIT,^{4,6} A. OZMEN,⁵
and M. YILMAZ^{2,7,8} 

1.—Department of Electrical and Electronics Engineering, Engineering Faculty, Sirnak University, 73000 Sirnak, Turkey. 2.—Advanced Materials Research Laboratory, Department of Nanoscience and Nanoengineering, Graduate School of Natural and Applied Sciences, Ataturk University, 25240 Erzurum, Turkey. 3.—Department of Physics, Science Faculty, Ataturk University, 25240 Erzurum, Turkey. 4.—Department of Electronics and Automation, Vocational High School, Bilecik Şeyh Edebali University, 11230 Bilecik, Turkey. 5.—Department of Electronics and Automation, Vocational High School, Agri Ibrahim Cecen University, 04100 Agri, Turkey. 6.—e-mail: kocyigita58@gmail.com. 7.—e-mail: mehmetyilmaz@atauni.edu.tr. 8.—e-mail: yilmazmehmet32@gmail.com

Undoped and Cr-doped zinc oxide (ZnO) thin films were deposited on the glass and *p*-Si substrates by the chemical spray pyrolysis technique. The films were characterized by x-ray diffractometry (XRD) and UV–visible spectrometry, and electrical characterization was achieved by using the films as an interfacial layer between the Au and *p*-Si. The XRD results confirmed the undoped and Cr-doped ZnO thin film crystalline structures. UV–visible spectra provided the transmittance plots and band gap energy values. *I*–*V* measurements were performed on the fabricated Au/ZnO/*p*-Si and Au/ZnO:Cr/*p*-Si devices to determine the effect of the ZnO interfacial layer on their performance. Various junction parameters, such as the ideality factor, barrier height, and series resistance, were calculated from the *I*–*V* measurements by various techniques, and have been discussed in detail. A 100-mW/cm² power intensity light was exposed on the Au/ZnO:Cr/*p*-Si device to see the photodiode behavior as well as to determine light sensitivity parameters such as photosensitivity and detectivity. The results highlight that the Au/ZnO:Cr/*p*-Si device can be thought of for optoelectronic applications.

INTRODUCTION

Zinc oxide is a II–IV group semiconductor with a 3.37-eV-wide direct bandgap and 60 meV large exciton binding energy, which can be used a wide range of applications from ultraviolet light-emitting devices to solar cells.^{1–3} 1D ZnO nanostructured crystals have excellent waveguide and ideal photonic crystal effects supporting light transmission and extraction, as well as allowing an enhanced band edge emission by plasmonic effects, making them electronically, optically, and magnetically efficient.^{4,5} Therefore, the production of ZnO semiconductors with desired properties is very

important. The characteristics of the synthesized semiconductor are directly dependent on the production method, and the characteristics of the semiconductor materials can be controlled by doping of other elements into the crystal lattice.⁶ For this reason, it is important to determine the correct doping element for the related semiconductor. For example, when the ZnO doped by III group elements, such as Al, Ga, and In, this treatment improves the optical properties, and thus the ZnO is more suitable for optoelectronic applications.^{7–9} The ZnO also provides the opportunity for making optical band engineering by using it in UV detectors and light emitters,^{10,11} as well as in photodiodes and photodetectors. In a study performed on a ZnO-based Au/ZnO:Co/*n*-Si device with transition element doping, the device exhibited a photovoltaic behavior, and the photoconductivity mechanism

(Received June 12, 2021; accepted December 8, 2021)

was controlled by the presence of a continuous distribution of cobalt-based traps.¹² In another study, Chey et al. examined the UV photodiode properties of a PEDOT:PSS/Mn-doped ZnO Schottky diode, and calculated the responsivity and fast response time values as 0.065 A/W and 2.75 s, respectively, as a result of the transition element contribution.¹³ Since chromium (Cr) has an ionic radius close to that of Zn^{2+} , it can easily enter the ZnO crystal lattice or replace Zn^{2+} in the crystal. This property makes it a good candidate as a dopant for improving ZnO film characteristics. Furthermore, there are numerous growing techniques in the literature to obtain ZnO thin films.^{14–16} Among these, the chemical spraying technique can be seen as more advantageous due to its simplicity, cheapness, ease of use, and ability to work without vacuum at low temperatures, but obtaining a uniform film structure can be hard due to the need to control the droplet size and the distribution of thermogravimetric forces.^{17,18} As mentioned above, due to the importance of transition metal-doped ZnO for device applications, it is important to investigate the performance of Cr-doped ZnO films as an interfacial layer obtained by the chemical spray pyrolysis technique in an Au/ZnO:Cr/*p*-Si device. Therefore, in this study, the aim has been to make an Au/ZnO:Cr/*p*-Si device more sensitive to light by reducing the band gap of the ZnO grown by chemical spraying with Cr doping. For this purpose, Au/ZnO:Cr/*p*-Si devices were fabricated and characterized by x-ray diffraction (XRD), an ultra-violet–visible light (UV–Vis) spectrometer, and current–voltage (*I*–*V*) measurements to try to find a correlation between the structural changes caused by Cr doping and the related variation in the junction parameters.

EXPERIMENTAL

For this study, undoped and Cr-doped ZnO thin films were obtained by chemical spray pyrolysis. Zinc acetate salt $[(\text{CH}_3\text{COO})_2\text{Zn} \cdot 2\text{H}_2\text{O}]$ purchased from Sigma-Aldrich as the main source for ZnO thin films was dissolved in a deionized water, isopropyl alcohol, and acetic acid mixed solution in a volumetric ratio of 3:5:2, respectively, and stirred in a magnetic stirrer at room temperature. The precursor solution for the Cr-doped ZnO was prepared by dropping the $\text{CrCl}_3 \cdot 6\text{H}_2\text{O}$ aqueous solution into the obtained ZnO solution with a ratio of 1:1 for a [Cr]/[Zn] percentage by weight. The precursor solutions prepared for the undoped and Cr-doped ZnO were sprayed onto both soda-lime glass and *p*-Si substrates that had previously been cleaned by the RCA process, and they reached the spraying temperature by chemical spray pyrolysis. Based on the studies in references,^{19,20} where the ZnO was obtained by chemical spray pyrolysis, the spraying temperature was determined as 450°C, with this temperature being measured by a k-type thermocouple with

$\pm 5^\circ\text{C}$ sensitivity. Other experimental parameters, such as the nozzle–substrate distance and the flow rate, were adjusted to 40 cm and 2 ml/min, respectively. Then, 20 ml of the solutions were sprayed onto the hot glass and *p*-Si substrates for 10 min at the same time, and the substrates were left to cool until they returned to room temperature. The thickness of the films was calculated by the weight differences method using a sensitive microbalance, and the thicknesses, which were almost the same, were found to be 300 nm and 305 nm for the undoped and Cr-doped ZnO films, respectively.

Film structures on the glass substrate were analyzed by XRD in the range of $2\theta = 20^\circ\text{--}80^\circ$ at room temperature. The optical properties of the films on glass substrate were carried out by UV–Vis spectrometer. The Au/ZnO/*p*-Si and Au/ZnO:Cr/*p*-Si devices were fabricated by a DC magnetron and thermal evaporation technique to evaporate of both the Au metallic front contact and the Al back ohmic contact, respectively. For this purpose, the Au contacts with the $7.85 \times 10^{-3} \text{ cm}^2$ contact area and 70 nm thickness were sputtered onto ZnO and ZnO:Cr films by using DC magnetron sputtering at 10^{-5} Torr. As the reference electrode or ohmic contact, the Al layer with 80 nm thicknesses was evaporated backside of the *p*-Si by thermal evaporation, and then the Al-coated samples were annealed in a N_2 -filled oven for 5 min. In this way, the Au/ZnO:Cr/*p*-Si devices were fabricated.

The XRD measurements were obtained by a PANalytical x-ray diffractometer with $\text{CuK}\alpha$ radiation ($\lambda = 1.54 \text{ }\mu\text{m}$) operated at 40 kV and 30 mA at room temperature. A Perkin Elmer UV–Vis spectrophotometer was employed to collect transmittance data from 200 nm to 800 nm, and a Keithley 2400 picoammeter was used for the *I*–*V* measurements with a Sciencetec (AM1.5 G and 300–1200 nm wavelength ranges) solar simulator.

RESULTS AND DISCUSSION

Structural Properties

The structural properties of the undoped and Cr-doped ZnO films obtained by the chemical spray pyrolysis method were analyzed by XRD, as shown in Fig. 1a and b for the doped and undoped ZnO, respectively. The XRD patterns of the samples are in good agreement with the data obtained from JCPDS card number of 36-1451, which indicates that the powder ZnO sample has a hexagonal wurtzite crystal structure. Furthermore, the high intensity of the (100), (002), and (101) planes, as well as the presence of the relatively lower intensity of the (102), (110), (103), and (112) planes, support the idea that the films have a hexagonal ZnO wurtzite structure according to the XRD pattern. Based on the XRD results, there are no extra peaks arising from chromium, other oxides, or any zinc chromium phase; only a single phase of the synthesized samples can be seen. Substitution of Zn^{2+}

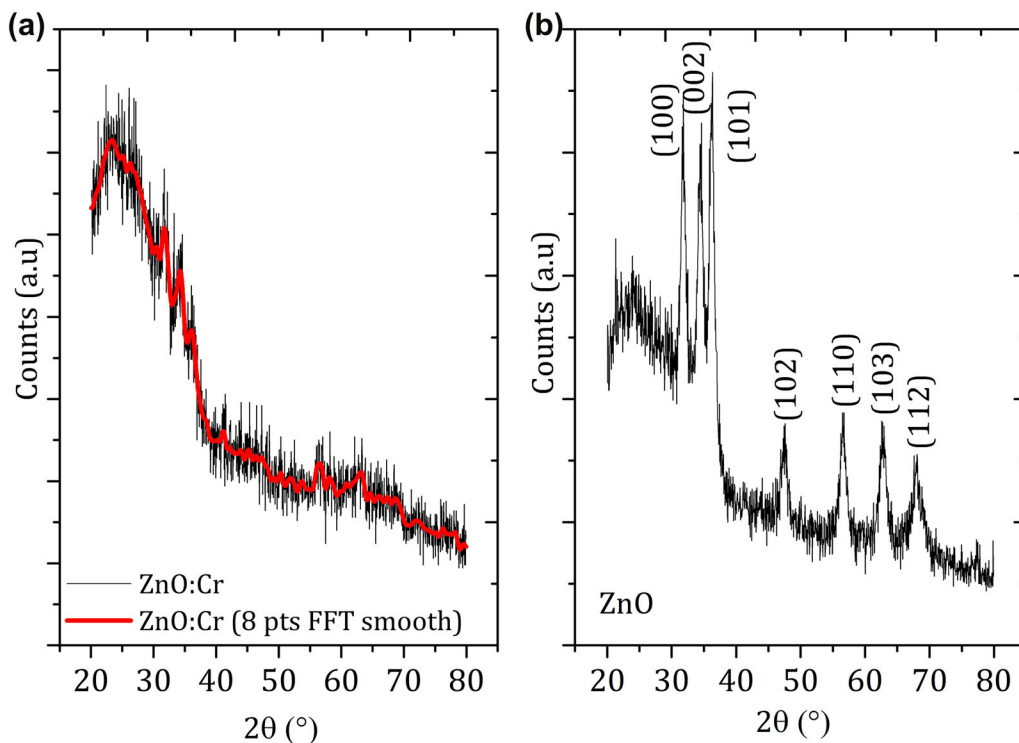


Fig 1. XRD pattern of the (a) ZnO:Cr and (b) ZnO thin films.

(0.74 Å) ions with Cr^{3+} (0.63 Å) ions causes deterioration of crystal quality due to the difference in ionic radii. This situation leads to a gradual decrease in the intensity of the peaks, indicating a deterioration in the crystal structure due to the increase in chromium content. Another reason for the deterioration of the crystal structure of ZnO is that the Cr atoms do not replace the O and Zn atoms, but instead occupy the interstitial regions.²¹ Hence, the presence of Cr in the structure causes strains, changes the lattice parameters, and thus deteriorates the crystal structure of ZnO, as seen in Fig. 1a. The XRD sample of the Cr-doped ZnO film is quite noisy. In some studies,^{22,23} it has been suggested to smooth the raw data for researchers to analyze such a sample properly. In this context, we used 8 pts smoothed XRD patterns to analysis for Cr-doped ZnO films. Smoothed data showed the presence of low intensity (100), (002), and (101) planes in Cr-doped ZnO film. The deterioration in the crystal lattice by doping of the ZnO films has also been observed in different studies.^{24,25} Moreover, variation in lattice parameters depending on Cr content may be related to microstrains generated by residual stress in the film.²⁶ The interplanar distance “ d ” values of the (100) and (101) planes obtained from XRD have been found to be 2.8208 Å and 2.4925 Å for the undoped ZnO film, while they were 2.8120 Å and 2.4698 Å for the Cr-decorated ZnO films, respectively. The lattice parameters for undoped and Cr-doped ZnO films have been calculated by following equation and determined as

($a = 3.257$ Å, $c = 5.323$ Å) and ($a = 3.247$ Å, $c = 5.165$ Å), respectively, by using the h , k , and l miller indices.²⁷

$$\frac{1}{d^2} = \frac{4}{3} \left(\frac{h^2 + k^2 + hk}{a^2} \right) + \left(\frac{l^2}{c^2} \right) \quad (1)$$

Considering the obtained results, there are decreases at the lattice constants of the ZnO due to the Cr contribution. The possible reason for the decrease at the lattice constants is that the ionic radius of the Cr^{3+} ions is lower compared to Zn^{2+} . Similar results have been observed in ZnO lattice constants for Cr-doped ZnO films by other researchers.^{28,29} Estimated crystallite sizes (D) of the undoped and Cr-doped ZnO thin films for high intensity peaks have been calculated with an error rate using the Scherrer formula, and are given in Table I.³⁰ Although the error rate of the Cr-doped sample was calculated to be high, the D value was found to be high for Cr-doped ZnO compared with the undoped one.

High-density peaks indicate that they increase the grain size in these directions by reducing the surface-free energy. Therefore, estimated particle size values have been obtained by considering the dominant peaks seen in the XRD samples for undoped and Cr-doped ZnO film samples. Thus, the estimated particle size exhibits an increasing tendency with the presence of Cr content. In the literature, it is possible to find studies showing that the estimated particle size of ZnO decreases^{31,32} and

Table I. Variation in some structural parameters of ZnO films in terms of Cr content

<i>hkl</i>	ZnO <i>D</i> (nm)	ZnO:Cr <i>D</i> (nm)	ZnO δ ($\times 10^{15}$ lines m^{-2})	ZnO:Cr δ ($\times 10^{15}$ lines m^{-2})
(100)	14.08	19.17	5.04	2.71
(002)	14.48	24.13	4.76	1.71
(101)	13.43	30.30	5.54	1.08
Average	13.99 ± 0.30	24.53 ± 3.21	5.11	1.83

increases,^{29,33} depending on the Cr contribution. Based on these studies, it can be concluded that a moderate amount of Cr content in ZnO thin films enhances the grain size. Equations 2 and 3 can be used to determine lattice strain (ε) and dislocation density (δ) of the films:^{30,34}

$$\varepsilon_s = \frac{(c - c_0)}{c_0} \times 100 \quad (2)$$

$$\delta = 1/D^2 \quad (3)$$

where c and c_0 are the strained and unstrained lattice constant, respectively. The lattice strain values have been calculated as 2.19 and -0.79 for the undoped and Cr-doped ZnO, respectively. As can be seen from the results, the lattice strain value turned from positive to negative depending on the Cr contribution. This may be attributed to the decrease in the lattice parameter “ c ” due to the Cr content. Although there are studies^{33,35} showing that high Cr content (as Cr_2O_3) can inhibit the growth of ZnO crystallites, and consequently the crystallite size will reduce, it is possible to see the opposite in practice.³⁶ This can be explained by the significant effect of Cr doping on the lattice strain by reducing the lattice parameter (c) of ZnO. The crystallite size has increased as seen here due to less stress caused by the decrease in the lattice constant. A decrease in the dislocation density values is observed in Table I, which indicates that the amount of defects in the structure has decreased.

Optical Properties

The band gap and transmittance spectra of the undoped and Cr-doped ZnO thin films grown by the chemical spray pyrolysis method are given in Fig. 2-a. As seen in the Fig. 2a inset, the optical transparency of both films is above 90% in the visible region. In the literature, there are studies^{37,38} showing that optical transmittance decreases because the increase of undesirable defects in thin films causes light scattering. On the contrary, the dislocation density value, which is a measure of the amount of defects in the structure, tends to decrease compared to the value of undoped ZnO. There are some improvements in the optical transmittance of

the Cr-doped film due to the reduction of the defect amounts which cause light scattering.

Furthermore, the optical transmittance spectra of the samples have exhibited sharp fundamental absorption edges indicating the optical band gap of the ZnO. This sudden drop in the optical transmittance spectra represents the electronic transition between the conduction and valence bands of the semiconductor. The result of the optical band structure reveals that direct transitions from band to band are allowed for ZnO, and this transition can be determined by the following expression:^{39,40}

$$(\alpha h\nu) = S(h\nu - E_g)^2 \quad (4)$$

where S and E_g represent the energy-dependent constant and optical band gap, respectively, and the α , h , and ν represent the absorption coefficient, Planck constant, and frequency, respectively. Considering Eq. 4, it is necessary to draw $(\alpha h\nu)^2$ versus $(h\nu)$ plots (Fig. 2a) to determine the optical band gap of the ZnO. Thus, the calculated optical band gap values have been calculated as 3.67 ± 0.0021 eV and 3.29 ± 0.0022 eV for the undoped and Cr-doped ZnO, respectively. This variation occurring at the optical band gap may be caused by factors such as film thickness, grain size, and change in structural parameters and by an increase at carrier concentration.⁴¹ However, this kind of band shrinkage in transition metal-doped II–IV semiconductors can be thought of as a result of the strong exchange interaction between the p and s electrons of the host band and the d electron of the Cr atoms.^{39,42,43} The XPS investigations have been carried out in order to evaluate the chemical state of the host and the dopant elements, and the existence of Zn, Cr, and O elements in chromium-doped ZnO film are shown in Fig. 2b, c, and d after base line correction, as shown in the literature.^{44,45} In the literature,⁴⁶ the peak values of Zn 2p_{3/2} and Zn 2p_{1/2} states for undoped ZnO were observed at 1021.6 eV and 1044.7 eV, respectively. In the XPS analysis (Fig. 2a) obtained for the Cr-doped ZnO thin film within the scope of our study, these values were observed at 1018.1 eV and 1041.3 eV, respectively. The fact that the 2p states observed for Cr-doped ZnO thin films are lower than for undoped ones indicates that there are considerable oxygen vacancies in the Cr-doped ZnO films. The binding energy of O1s may be calculated by dividing the peaks seen

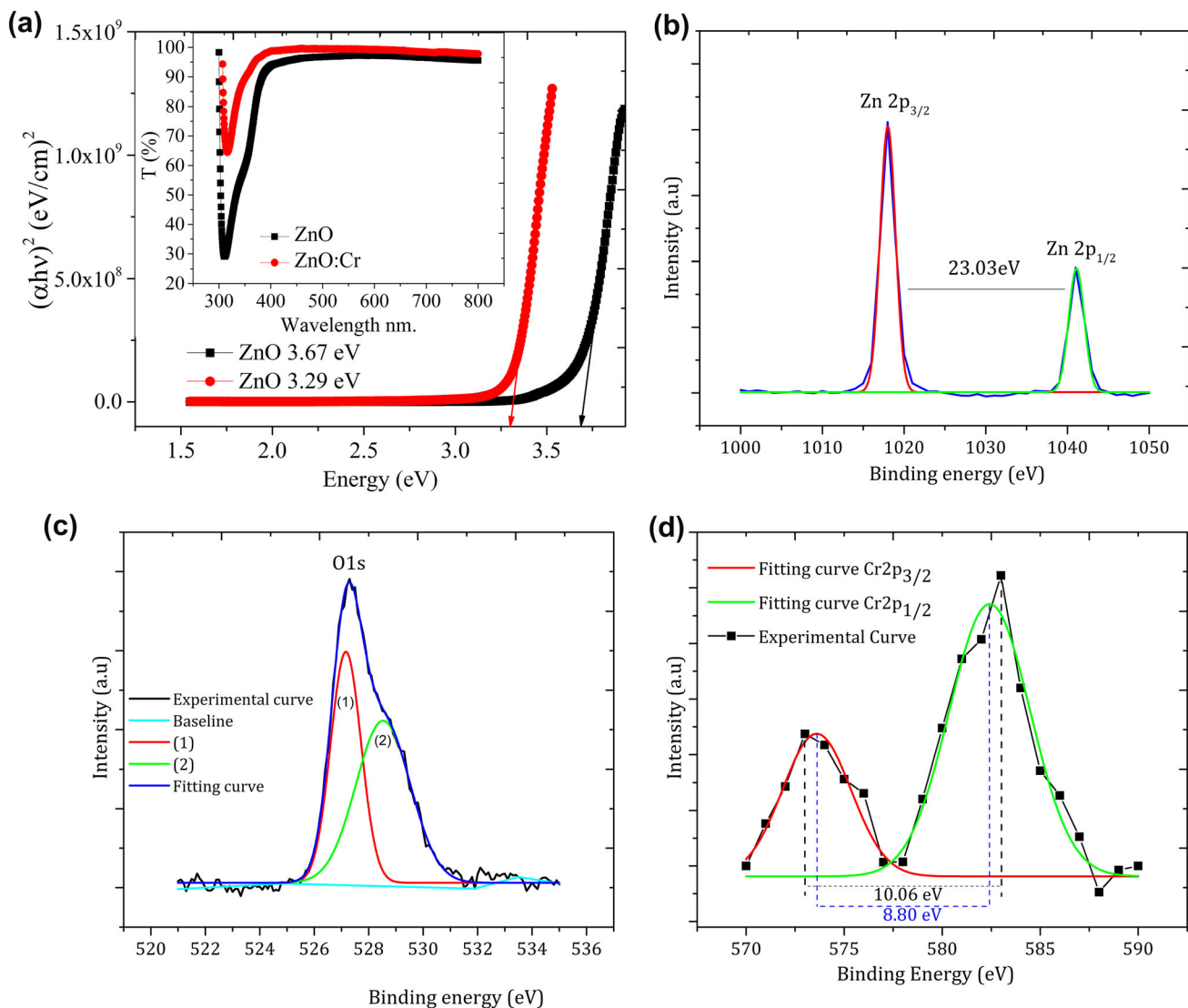


Fig 2. (a) Transmittance spectra and the plot of $(\alpha h\nu)^2$ versus $(h\nu)$ of ZnO:Cr films, and (b-d) XPS spectra of ZnO:Cr films.

in Fig. 2c by (1) and (2). The first of these, at 527.1 eV, is attributable to chemically absorbed oxygen species (O_2^-) in the Zn–O bond of the ZnO wurtzite structure, while the second, at 528.5 eV, is connected with oxygen-deficient areas (O^- and O_2^- ions) in the sample matrix. Similar observations have been made by other researchers^{47,48} with a slightly differences and also different semiconductors. Figure 2d depicts the sample's Cr 2p_{3/2} and Cr 2p_{1/2} XPS spectral areas. Also, the position of the Cr 2p_{3/2} peak has been observed to be slightly different compared with the Cr metal (574.2 eV). In addition, in general, if Cr is present in the substitution site of a defect-free ZnO crystal, the valence state is expected to be + 2. However, although the Cr 2p_{3/2}–Cr 2p_{1/2} peaks were observed in slightly different places from those in the literature, the peak separations are consistent with the literature.^{49–51} This confirms the hypothesis that the chromium ions are in the + 3 valence state in the ZnO lattice structure.

Electrical Properties

The fabricated Au/ZnO/p-Si and Au/ZnO:Cr/p-Si devices were characterized by *I*–*V* measurements both for determining various junction parameters, such as ideality factor (*n*), barrier height (Φ_b), and series resistance (*R_s*), and for understanding the current conduction mechanism. Figure 3a shows the *I*–*V* characteristics of the Au/ZnO/p-Si and Au/ZnO:Cr/p-Si devices, and it contains the *I*–*V* characteristics of the Au/ZnO:Cr/p-Si device under 100-mW/cm² light power illumination. The Au/ZnO/p-Si device has a minimum current at 0 V, but the current increased slowly with increasing reverse biases and stayed constant or saturated at around – 0.7 V. This slow saturating with increasing reverse biases can be attributed to the reduction of the barrier height.⁵² This feature may be important for a better gas-sensing device, as forward or reverse bias can provide information about

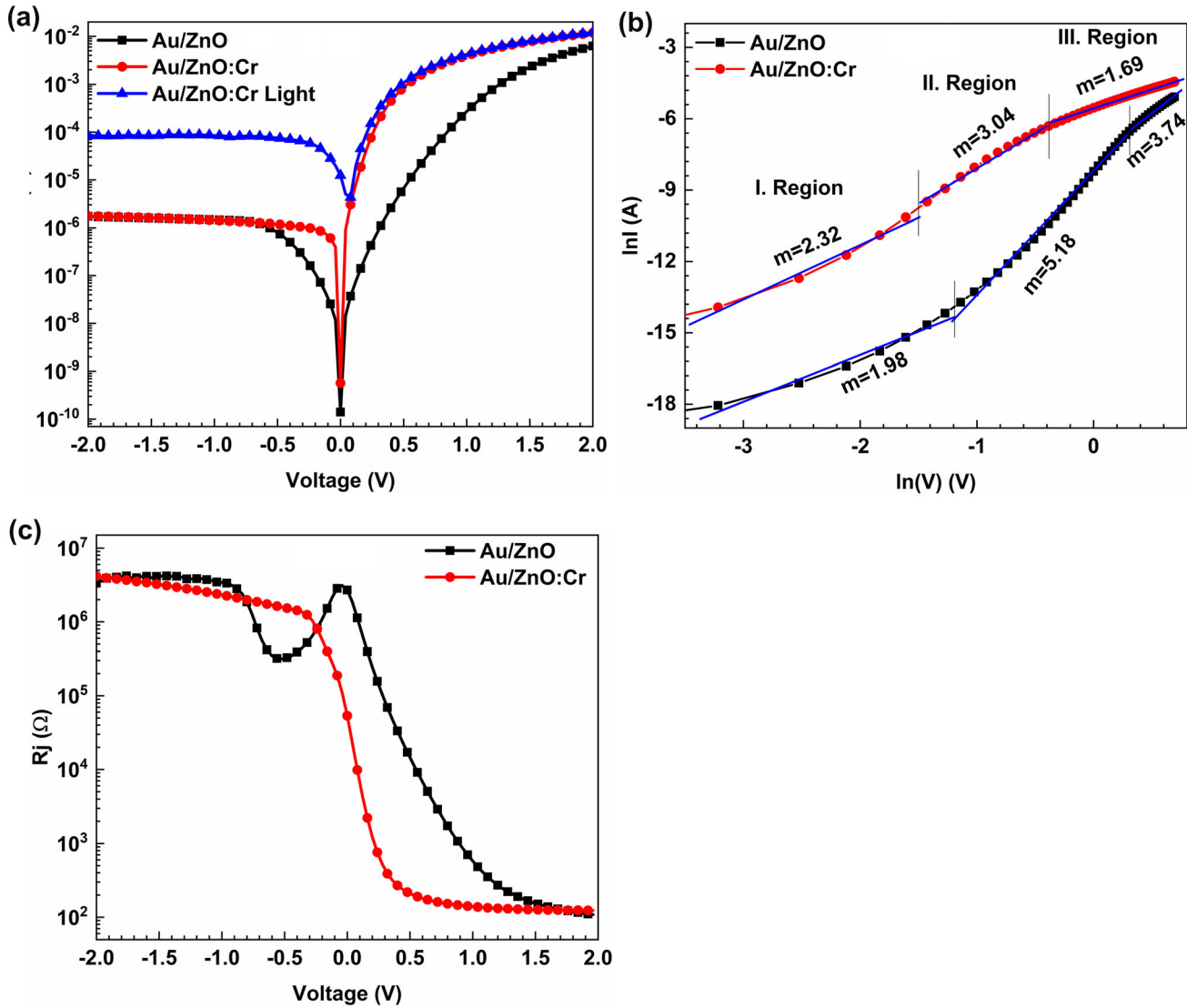


Fig 3. (a) I - V characteristics, (b) $\ln I$ - $\ln V$ graphs, and (c) R_j - V plots of the Au/ZnO/ p -Si and Au/ZnO:Cr/ p -Si devices.

alternative gas-sensing features.⁵³ The Cr-doped ZnO interface layered Au/ZnO:Cr/ p -Si device immediately reached saturated current values at reverse biases due to the increase of the charge carriers with Cr doping, because the charge carriers were not trapped and immediately had a response to the reverse biases. The Au/ZnO:Cr/ p -Si device has 100 times higher current values at reverse biases under 100-mW/cm^2 light illumination power than in dark conditions. This result confirms the photodiode behavior of the Au/ZnO:Cr/ p -Si device.

The rectifying ratio (RR) values, which are important for this kind of junction device, are listed in Table II. The RR values of the Au/ZnO/ p -Si, Au/ZnO:Cr/ p -Si (under dark), and Au/ZnO:Cr/ p -Si (under light illumination) devices were calculated to be 3.64×10^3 , 6.70×10^3 , and 1.43×10^2 , respectively, at ± 2 V. The RR value slightly increased with the doping of the Cr into the ZnO interfacial layer because Cr doping caused an increase of the

forward bias current. When the Au/ZnO:Cr/ p -Si device was illuminated with light, the RR value decreased to 1.43×10^2 due to increasing reverse bias current. Both the obtained RR values and the reverse bias photocurrent by light illumination confirm the photodiode behavior of the Au/ZnO:Cr/ p -Si device. Furthermore, there is an increase and a slight shift towards the forward bias region in the current of the Au/ZnO:Cr/ p -Si device after illumination, due to the generation of the excitons by the light at the interface.⁵⁴ The forward current level did not change so much with the illumination of the Au/ZnO:Cr/ p -Si device at the forward biases, because the applied voltage was more effective than the light power illumination at forward biases for this kind of junction structure. This result can be found easily in the literature for metal semiconductor contacts.^{55,56} The detection parameters, such as the responsivity, photosensitivity, and detectivity values, of the Au/ZnO:Cr/ p -Si device were

Table II. The calculated junction parameters of the Au/ZnO/p-Si and Au/ZnO:Cr/p-Si devices

Device	Saturation current (I_0) (A)	n (TE) –	n Cheung –	Φ_b (TE) (eV)	Φ_b Cheung (eV)	Φ_b Norde (eV)	R_s Norde (k Ω)	R_s Cheung (k Ω (dln(I)))	R_s Cheung (k Ω ($H(I)$))	RR (at ± 2 V)
Au/ZnO	2.64×10^{-8}	3.65	3.86	0.71	0.70	0.78	2.39	1.24	1.23	3.64×10^3
Au/ZnO:Cr	3.85×10^{-7}	1.76	1.78	0.64	0.75	0.68	44.01	0.35	0.20	6.70×10^3
Au/ZnO:Cr Light	1.08×10^{-6}	2.08	2.18	0.61	0.71	0.62	56.16	0.21	0.19	1.43×10^2

calculated for 100-mW/cm² light power intensity, and were 1.57 A/W, 2.17×10^4 , and 1.03×10^{13} Jones, respectively. These optoelectronic parameters are high and so suitable for optoelectronic applications for ZnO-based devices according to the literature.⁵⁷

The current conduction mechanism of the Au/ZnO/p-Si and Au/ZnO:Cr/p-Si devices was characterized by plotting the $\ln I$ – $\ln V$ graphs from the I – V data. The $\ln I$ – $\ln V$ graphs of the Au/ZnO/p-Si and Au/ZnO:Cr/p-Si devices are shown in Fig. 3b, and exhibit three distinct regions for both the devices depending on the $I = bV^m$ relationship. While the b is constant, the m is another constant for determining the current conduction mechanism. If m changes between 1 and 2, the device has a Schottky emission or a Poole–Frenkel conduction mechanism. If m is greater than 2, the device has a trapped or surface charge-limited current mechanism.^{58,59} The Au/ZnO/p-Si device has a Schottky emission or a Poole–Frenkel conduction mechanism in the low-voltage region. In the higher-voltage regions, the device has a space charge-limited current mechanism. In the case of the Au/ZnO:Cr/p-Si device, the device has a trapped and a space charge-limited current mechanism in the first and second regions, but a Schottky emission or a Poole–Frenkel conduction mechanism are effective in the higher-voltage region. The differences in the changes in the current conduction mechanism can be attributed to the injection of charges to the current after the Cr doping to the ZnO interfacial layer.⁶⁰

Junction resistance (R_j) is important for affecting the I – V characteristics, and it contains both the series (R_s) and shunt resistance (R_{sh}).⁶¹ While the interfacial layer, wires, etc. causes series resistance, the contact–semiconductor interface causes the shunt resistance.⁶² The R_j is calculated by:

$$R_j = \frac{\partial V}{\partial I} \quad (5)$$

Figure 3c shows the R_j – V plots of the Au/ZnO/p-Si and Au/ZnO:Cr/p-Si devices. While the series

resistance is determined from the forward biases, the shunt resistance is obtained from the reverse biases.⁶³ In the case of the Au/ZnO/p-Si device, both the R_s and R_{sh} values have changing values with changing bias. The R_s values first decreased linearly after exponentially decreasing and reached almost stable values at about 123 Ω . The R_{sh} values fluctuated towards -1 V and stayed constant at around $3.95 \times 10^6 \Omega$ after this bias value. In the case of the Au/ZnO:Cr/p-Si device, the R_s values suddenly decreased and stayed constant at around 124 Ω . The R_{sh} values slightly increased towards -2 V and reached $4.17 \times 10^6 \Omega$. While the Au/ZnO/p-Si has a changeable series and shunt resistance with changing bias, the Au/ZnO:Cr/p-Si device has a more stable series and shunt resistance. This case can be attributed to the Cr doped to the ZnO passivated dangling bonds and ionic traps. Furthermore, the R_s and R_{sh} values are suitable for optoelectronic applications and comparable with the literature for ZnO-based devices.^{64–66}

Using thermionic emission (TE) theory, Norde and Cheung methods can be used to determine various junction parameters. TE theory helps to calculate the barrier height and ideality factor from I – V measurements. The current (I) is, according to TE, given as:

$$I = I_0 \exp\left(\frac{qV}{nkT}\right) \left[1 - \exp\left(-\frac{qV}{nkT}\right)\right] \quad (6)$$

where I_0 represents the saturation current and is calculated by:

$$I_0 = AA^*T^2 \exp\left(-\frac{q\Phi_b}{kT}\right) \quad (7)$$

where q is the charge of the electron, k is Boltzmann's constant, and V is the applied bias voltage, A^* , A , and T show the Richardson constant, contact area ($A = 7.85 \times 10^{-3}$ cm²), and temperature, respectively. For $V \geq 3kT/q$, the n and Φ_b are obtained by:

$$n = \frac{q}{kT} \left(\frac{dV}{d \ln I} \right) \quad (8)$$

and

$$\Phi_b = \frac{kT}{q} \ln \left(\frac{A^* A T^2}{I_0} \right) \quad (9)$$

The calculated ideality factor and barrier height values are listed in Table II for the Au/ZnO/*p*-Si and Au/ZnO:Cr/*p*-Si devices as well as the light-illuminated Au/ZnO:Cr/*p*-Si device. The ideality factor value decreased from 3.65 to 1.76 with the Cr-doped ZnO layer, and the barrier height value also decreased from 0.71 eV to 0.64 eV. This can be because the Cr doping into the ZnO interfacial layer may cause a decrease in the series resistance and interface states, or can depend on the deviation from the thermionic emission conduction mechanism due to current flow.^{67,68} The illumination increased in the ideality factor from 1.76 to 2.08, but the barrier height decreased from 0.64 eV to 0.61 eV in the Au/ZnO:Cr/*p*-Si device. This increase in the ideality factor and decrease in the barrier height with illumination can be attributed to the slight increase in the current at forward biases due to illumination. The calculated ideality factor and barrier height values are in good agreement with the literature for ZnO-based photodiodes.⁶⁹

The Norde method can be employed to calculate the R_s and to check the accuracy of the Φ_b values. The Norde function is calculated and given by the next formula depending on the voltage (V) and the voltage-dependent current $I(V)$:^{70,71}

$$F(V) = \frac{V}{\gamma} - \frac{kT}{q} \ln \left(\frac{I(V)}{AA^*T^2} \right) \quad (10)$$

where γ is a larger integer value than the TE theory n . The Φ_b and R_s formulae are extracted from the Norde function and given by:

$$\Phi_b = F(V_0) + \left[\frac{V_0}{\gamma} - \frac{kT}{q} \right] \quad (11)$$

$$R_s = \frac{\gamma - n}{I} \frac{kT}{q} \quad (12)$$

where V_0 shows the minimum voltage value depending on the minimum $F(V)$ value.

Figure 4 displays $F(V)$ - V graphs of the Au/ZnO/*p*-Si and Au/ZnO:Cr/*p*-Si devices. The graphs exhibit normal Norde function graphs. The Φ_b and R_s values are tabulated in Table II. While the Φ_b values are compatible with TE theory calculation, R_s values are calculated as 2.39 k Ω , 44.01 k Ω , and 56.16 k Ω for the Au/ZnO/*p*-Si, Au/ZnO:Cr/*p*-Si, and Au/ZnO:Cr/*p*-Si (under light exposure) devices, respectively. The reason is that the high-value R_s rather than the junction R_s value can be attributed to approximation differences or using different

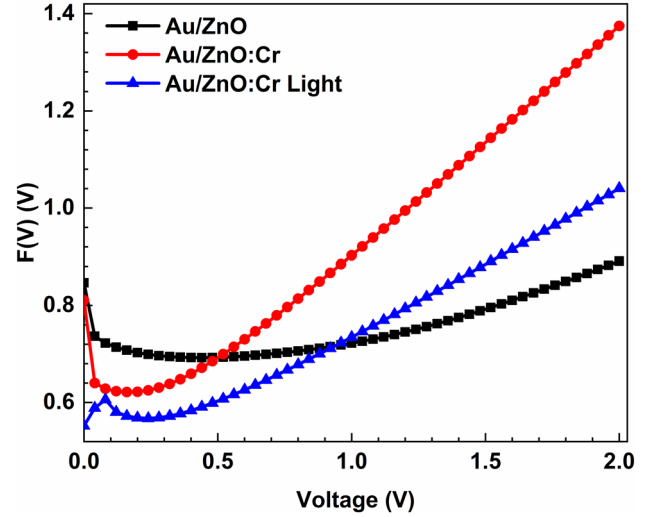


Fig. 4. $F(V)$ - V graphs of the Au/ZnO/*p*-Si and Au/ZnO:Cr/*p*-Si devices.

regions of the semi-logarithmic I - V plots as well as a non-ideal junction structure.^{72,73}

The ideality factor, barrier height, and series resistance can be determined by the Cheung method to compare and confirm other methods' device parameters.⁷⁴ The Cheung technique gives the current as the following equation depending on voltage and voltage drops (IR_s) due to series resistance:

$$I = I_0 \exp \left(-\frac{q(V - IR_s)}{nkT} \right) \quad (13)$$

With the help of Eq. 12, Cheung functions can be obtained:

$$\frac{dV}{d(\ln I)} = IR_s + n \frac{kT}{q} \quad (14)$$

$$H(I) = V - n \left(\frac{kT}{q} \right) \ln \left(\frac{I}{AA^*T^2} \right) \quad (15)$$

where $H(I)$ can be rearranged as:

$$H(I) = IR_s + n\Phi_b \quad (16)$$

Both the $dV/d(\ln I)$ and $H(I)$ functions are linear equations and give a straight line when plotted against I . From these plots, the n , Φ_b , and two R_s values can be calculated.^{75,76} Figure 5a and b display the $dV/d(\ln I)$ and $H(I)$ versus I plots of the Au/ZnO/*p*-Si and Au/ZnO:Cr/*p*-Si devices, respectively. Both $dV/d(\ln I)$ and $H(I)$ versus I plots exhibit good linearity. The junction parameters are listed in Table II for the Au/ZnO/*p*-Si, Au/ZnO:Cr/*p*-Si and Au/ZnO:Cr/*p*-Si (under light condition) devices. While the ideality factor is in good agreement with the results of the TE theory values, the barrier height values are not compatible with both the Norde and TE theory method values. Furthermore,

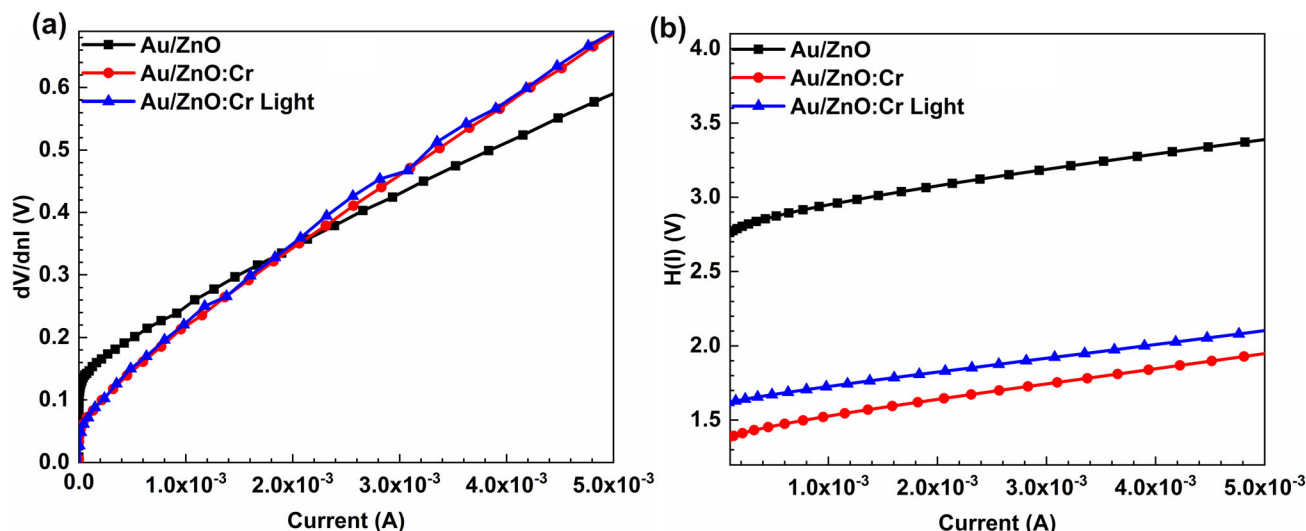


Fig 5. (a) $dV/d(\ln I)$ – and (b) $H(I)$ – I plots of the Au/ZnO/ p -Si, Au/ZnO:Cr/ p -Si, and Au/ZnO:Cr/ p -Si (under light) devices.

there are big differences for the R_s values in these two methods. The reason for this discrepancy can be attributed to the determining regions of the Φ_b in the I – V characteristics and the non-ideal junction structure.⁷⁷ The R_s values of the Au/ZnO/ p -Si, Au/ZnO:Cr/ p -Si, and light exposure Au/ZnO:Cr/ p -Si devices have been determined as 1.24 k Ω , 0.35 k Ω , and 0.21 k Ω for $dV/d(\ln I)$, respectively. According to these results, the R_s values decreased with the doping of the Cr to the ZnO interfacial layer. The light illumination on the Au/ZnO:Cr/ p -Si device also caused a slight decrease in the R_s value. The differences in the R_s values from these techniques can be attributed to changing the current curve with the changing voltage values too much.

CONCLUSION

The undoped and Cr-doped ZnO thin films were fabricated on glass substrates as well as p -Si by a chemical spray pyrolysis technique. The films on the glass were characterized by XRD and UV–visible spectrometry. The XRD results revealed the undoped and Cr-doped ZnO crystalline structures in nature. Various structural parameters, such as crystalline size, lattice constants, and dislocation density, as well as strain values, were extracted from the XRD data and have been discussed in detail for the undoped and Cr-doped ZnO films. UV–visible spectra exhibited a high transmittance value above 90%. The band gap values of the undoped and Cr-doped ZnO were 3.67 eV and 3.29 eV, respectively. The electrical characterization was achieved by depositing the films as an interfacial layer between the Au and the p -Si. I – V measurements were performed on the Au/ZnO/ p -Si and Au/ZnO:Cr/ p -Si devices to determine the effect of the ZnO interfacial layer on their performance. The ideality factor values were 3.65 for the Au/ZnO/ p -Si, 1.76 for the Au/ZnO:Cr/ p -Si, and 2.08 for the Au/ZnO:Cr/ p -Si devices under light illumination.

The barrier height values were calculated as 0.71 eV, 0.64 eV, and 0.61 eV for the Au/ZnO/ p -Si, Au/ZnO:Cr/ p -Si, and light exposure Au/ZnO:Cr/ p -Si devices, respectively. The series resistance values were also calculated from the I – V measurements by various techniques and have been discussed in detail. The devices exhibited high RR values, but their values changed by changing both the Cr doping and the illumination. The Au/ZnO:Cr/ p -Si device exhibited good photodiode behavior, high responsivity, photo-sensitivity, and detectivity at 100-mW/cm² power intensity light. These results highlight that the Au/ZnO:Cr/ p -Si device can be considered suitable for optoelectronic applications.

ACKNOWLEDGEMENTS

The authors would like to thanks Dr. Hatice Kacus for her technical support in this research. This study was supported by Sirnak University Research fund with Project Number 2021.FNAP.06.02.01.

CONFLICT OF INTEREST

The authors declare that they have no conflict of interest.

REFERENCES

1. M.A. Boda, B. BozkurtÇirak, Z. Demir, and Ç. Çirak, *Mater. Lett.* 248, 143 (2019).
2. B. BozkurtÇirak, Ç. Eden, Y. Erdoğan, Z. Demir, K.V. Öz-dokur, B. Caglar, S. MorkoçKaradeniz, T. Kılınc, A. ErcanEkinci, and Ç. Çirak, *Optik Stuttg.* 203, 163963 (2020).
3. D.C. Look, *Mater. Sci. Eng. B* 80, 383 (2001).
4. B. Wang, J. Iqbal, X. Shan, G. Huang, H. Fu, R. Yu, and D. Yu, *Mater. Chem. Phys.* 113, 103 (2009).
5. S.G. Zhang, L. Wen, J.L. Li, F.L. Gao, X.W. Zhang, L.H. Li, and G.Q. Li, *J. Phys. D* 47, 495103 (2014).
6. M. Yilmaz and M.L. Grilli, *Philos. Mag.* 96, 2125 (2016).
7. Y.-K. Tseng, G.-J. Gao, and S.-C. Chien, *Thin Solid Films* 518, 6259 (2010).
8. M. Yilmaz, *Mater. Sci. Semicond. Process.* 40, 99 (2015).

9. E.J. Luna-Arredondo, A. Maldonado, R. Asomoza, D.R. Acosta, M.A. Meléndez-Lira, and M. de la L. Olvera, *Thin Solid Films*, 490, 132 (2005).
10. D.P. Joseph and C. Venkateswaran, *J. At. Mol. Opt. Phys.* 2011, 1 (2011).
11. S. Senthilkumaar, K. Rajendran, S. Banerjee, T.K. Chini, and V. Sengodan, *Mater. Sci. Semicond. Process.* 11, 6 (2008).
12. F. Yakuphanoglu, *J. Alloys Compd.* 494, 451 (2010).
13. C.O. Chey, X. Liu, H. Alnoor, O. Nur, and M. Willander, *Phys. Status Solidi Rapid Res. Lett.* 9, 87 (2015).
14. S. Benramache, *Ann. West Univ. Timisoara Phys.* 61, 64 (2019).
15. N. Kumari, S.R. Patel, and J.V. Gohel, *Opt. Quantum Electron.* 50, 180 (2018).
16. F.K. Shan, B.C. Shin, S.W. Jang, and Y.S. Yu, *J. Eur. Ceram. Soc.* 24, 1015 (2004).
17. A. Özmen, S. Aydogan, and M. Yilmaz, *Ceram. Int.* 45, 14794 (2019).
18. J. Cho, S. Hwang, D.H. Ko, and S. Chung, *Materials* 12, 3423 (2019).
19. A. Maldonado, S.A. Mallen-Hernandez, and J. Vega-Perez, *Rev. Mex. Física* 55, 90 (2009).
20. A. Maldonado, M. de la L. Olvera, R. Asomoza, and S. Tirado-Guerra, *J. Vac. Sci. Technol. A*, 18, 2098 (2000).
21. S. Yilmaz, M. Parlak, Ş Özcan, M. Altunbaş, E. McGlynn, and E. Bacaksız, *Appl. Surf. Sci.* 257, 9293 (2011).
22. K. Frost, D. Kaminski, G. Kirwan, E. Lascaris, and R. Shanks, *Carbohydr. Polym.* 78, 543 (2009).
23. M. Yilmaz, A. Kocyigit, S. Aydogan, U. Incekara, Y. Sahin, and H. Kacus, *Appl. Phys. A* 126, 1 (2020).
24. A.R. Khantoul, M. Sebais, B. Rahal, B. Boudine, and O. Halimi, *Acta Phys. Pol. A* 133, 114 (2018).
25. F. Yakuphanoglu, Y. Caglar, S. Ilcan, and M. Caglar, *Phys. B* 394, 86 (2007).
26. M. Miki-Yoshida, F. Paraguay-Delgado, W. Estrada-López, and E. Andrade, *Thin Solid Films* 376, 99 (2000).
27. M. Shaban, and A.M. El Sayed, *Mater. Sci. Semicond. Process.* 39, 136 (2015).
28. V.D. Mote, V.R. Huse, and B.N. Dole, *World J. Condens. Matter Phys.* 02, 208 (2012).
29. A. Iqbal, A. Mahmood, T. Muhammad Khan, and E. Ahmed, *Prog. Nat. Sci. Mater. Int.* 23, 64 (2013).
30. M. Rajasekaran, A. Arunachalam, and P. Kumaresan, *Mater. Res. Express* 7, 036412 (2020).
31. O. Gürbüz and M. Okutan, *Appl. Surf. Sci.* 387, 1211 (2016).
32. W. Jin, I.-K. Lee, A. Kompch, U. Dörfler, and M. Winterer, *J. Eur. Ceram. Soc.* 27, 4333 (2007).
33. N.H. Al-Hardan, M.J. Abdullah, and A.A. Aziz, *Appl. Surf. Sci.* 270, 480 (2013).
34. J. Huo, W. Li, and T. Wang, *Coatings* 9, 376 (2019).
35. Y. Liu, J. Yang, Q. Guan, L. Yang, Y. Zhang, Y. Wang, B. Feng, J. Cao, X. Liu, Y. Yang, and M. Wei, *J. Alloys Compd.* 486, 835 (2009).
36. Z.N. Kayani, M. Siddiq, S. Riaz, and S. Naseem, *Mater. Res. Express* 4, 096403 (2017).
37. X. Du, J. Li, and X. Bi, *J. Alloys Compd.* 698, 128 (2017).
38. G. Jo and J.-H. Koh, *Ceram. Int.* 45, 6190 (2019).
39. H. Aydın, C. Aydın, A.A. Al-Ghamdi, W.A. Farooq, and F. Yakuphanoglu, *Optik* 127, 1879 (2016).
40. R.S. Ajimsha, A.K. Das, B.N. Singh, P. Misra, and L.M. Kukreja, *Phys. B* 406, 4578 (2011).
41. S.A. Ansari, F. Alam, A. Khan, W. Khan, M. Chaman, M. Muneer, and A.H. Naqvi, *Curr. Nanosci.* 8, 581 (2012).
42. M. Yilmaz and Ş Aydoğan, *Metall. Mater. Trans. A* 46, 2726 (2015).
43. Y.M. Hu, Y.T. Chen, Z.X. Zhong, C.C. Yu, G.J. Chen, P.Z. Huang, W.Y. Chou, J. Chang, and C.R. Wang, *Appl. Surf. Sci.* 254, 3873 (2008).
44. C.V. Ramana, S. Roy, V. Zade, A.K. Battu, N. Makeswaran, and V. Shutthanandan, *J. Phys. Chem. Solids* 157, 110174 (2021).
45. C.V. Ramana, M. Massot, and C.M. Julien, *Surfaces Interface Analysis* (Wiley, New York, 2005), pp 412–416.
46. S.S. Li and Y.K. Su, *RSC Adv.* 9, 2941 (2019).
47. N. Joshi, L.F. da Silva, F.M. Shimizu, V.R. Mastelaro, J.C. M'Peko, L. Lin, and O.N. Oliveira, *Microchim. Acta* 186, 1 (2019).
48. S. Manandhar, A.K. Battu, S. Tan, R. Panat, V. Shutthanandan, and C.V. Ramana, *J. Mater. Sci.* 54, 11526 (2019).
49. S. Wang, W. Bo, M. Zhong, C. Liu, Y. Li, M. Zhu, Y. Hu, and H. Jin, *J. Nanomater.* 2012, 1 (2012).
50. N. Neykova, Y.Y. Chang, M. Buryi, M. Davydova, R. Kucerkova, D. Simek, Z. Remes, and O. Pop-Georgievski, *Appl. Surf. Sci.* 472, 105 (2019).
51. S.C. Wang, H.T. Lin, P.K. Nayak, S.Y. Chang, and J.L. Huang, *Thin Solid Films* 518, 7360 (2010).
52. K.R. Peta and M.D. Kim, *Superlatt. Microstruct.* 113, 678 (2018).
53. D. Tomer, S. Rajput, L.J. Hudy, C.H. Li, and L. Li, *Appl. Phys. Lett.* 106, 173510 (2015).
54. A. Kocyigit, I. Orak, İ Karteri, and S. Urus, *Curr. Appl. Phys.* 17, 1215 (2017).
55. A. Kocyigit, M.O. Erdal, F. Ozel, and M. Yıldırım, *Nanotechnology* 32, 385204 (2021).
56. H.H. Gullu, D.E. Yildiz, A. Kocyigit, and M. Yıldırım, *J. Alloys Compd.* 827, 154279 (2020).
57. B. DekaBoruah, *Nanoscale Adv.* 1, 2059 (2019).
58. B. Tatar, A.E. Bulgurcuoglu, P. Gokdemir, P. Aydogan, D. Yilmazer, O. Ozdemir, and K. Kutlu, *Int. J. Hydrog. Energy* 34, 5208 (2009).
59. İ Orak, A. Kocyigit, and Ş Karataş, *Silicon* 10, 2109 (2018).
60. Ş Karataş, Ş Altındal, A. Türüt, and A. Özmen, *Appl. Surf. Sci.* 217, 250 (2003).
61. L.D. Rao and V.R. Reddy, in *AIP Conference Proceedings* (AIP Publishing, 2016), p. 120020.
62. F. Yakuphanoglu, *Sens. Actuators A* 141, 383 (2008).
63. U. Aydemir, I. Taşcıoğlu, Ş Altındal, and I. Uslu, *Mater. Sci. Semicond. Process.* 16, 1865 (2013).
64. İ Taşcıoğlu, W.A. Farooq, R. Turan, Ş Altındal, and F. Yakuphanoglu, *J. Alloys Compd.* 590, 157 (2014).
65. F.Z. Bedia, A. Bedia, B. Benyoucef, and S. Hamzaoui, *Physics Procedia* (Elsevier, Amsterdam, 2014), pp 61–67.
66. E. Aldirmaz, M. Güler, E. Güler, A. Dere, A. Tataroglu, and F. Yakuphanoglu, *Sens. Actuators A* 331, 112908 (2021).
67. A.A.M. Farag, M. Cavas, and F. Yakuphanoglu, *Mater. Chem. Phys.* 132, 550 (2012).
68. A.A. Hendi, and F. Yakuphanoglu, *J. Alloys Compd.* 665, 418 (2016).
69. I. Orak, A. Kocyigit, and A. Turut, *J. Alloys Compd.* 691, 873 (2017).
70. İ Orak, K. Ejderha, and A. Turut, *Curr. Appl. Phys.* 15, 1054 (2015).
71. H. Norde, *J. Appl. Phys.* 50, 5052 (1979).
72. D.A. Aldemir, *Mod. Phys. Lett. B* 34, 66 (2020).
73. M. Yilmaz, A. Kocyigit, B.B. Cirak, H. Kacus, U. Incekara, and S. Aydogan, *Mater. Sci. Semicond. Process.* 113, 105039 (2020).
74. S.K. Cheung and N.W. Cheung, *Appl. Phys. Lett.* 49, 85 (1986).
75. Ş Karataş, *Microelectron. Eng.* 87, 1935 (2010).
76. A. Kocyigit and I. Orak, *J. Inst. Sci. Technol.* 6, 57 (2016).
77. A. Tataroglu, Ş Altındal, and Y. Azizian-Kalandaragh, *Phys. B* 576, 411733 (2020).